https://doi.org/10.1016/j.compgeo.2021.104311

A New Soil Reaction Model for Large-diameter Monopiles in Clay

Guangwei Cao, Xuanming Ding*, Zhenyu Yin, Hang Zhou, Peng Zhou

Guangwei Cao

Ph.D Candidate

Key Laboratory of New Technology for Construction of Cities in Mountain Area, Chongqing University, College of Civil Engineering, Chongqing, 400045, China.

E-mail: m_ma123@163.com

Xuanming Ding (Corresponding author)

Professor (Ph.D)

Key Laboratory of New Technology for Construction of Cities in Mountain Area, Chongqing University, College of Civil Engineering, Chongqing, 400045, China.

E-mail: dxmhhu@163.com

Zhenyu Yin

Professor (Ph.D)

Department of Civil and Environmental Engineering, The Hong Kong Polytechnic University, Hung Hom, Kowloon, Hong Kong, China.

Email: zhenyu.yin@polyu.edu.hk

Hang Zhou

Associate Professor (Ph.D)

Key Laboratory of New Technology for the Construction of Cities in Mountain Areas, College of Civil Engineering, Chongqing University, Chongqing, 400045, China.

E-mail: zh4412517@163.com

Peng Zhou

Ph.D Candidate

Key Laboratory of New Technology for the Construction of Cities in Mountain Areas, College of Civil Engineering, Chongqing University, Chongqing, 400045, China.

E-mail: zhoupeng280217901@163.com

A New Soil Reaction Model for Large-diameter Monopiles in Clay

Guangwei Cao[1,2], Xuanming Ding[1,2]*, Zhenyu Yin[3], Hang Zhou[1,2], Peng Zhou[1,2]

1. College of Civil Engineering, Chongqing University, Chongqing, 400045, China.

2. Key Laboratory of New Technology for Construction of Cities in Mountain Area, Chongqing University, Chongqing 400045, China

3. Department of Civil and Environmental Engineering, The Hong Kong Polytechnic University, Hung Hom, Kowloon, Hong Kong, China.

Abstract: Considering the limits of the traditional *p*-*y* method and the omission of the non-negligible additional lateral resistance components for large-diameter monopiles, the effects of rotational soil flow and pile tip lateral components on the soil-pile lateral behavior are discussed in detail. A new unified soil reaction model is proposed to obtain a more accurate prediction of the lateral behavior of monopiles supporting offshore wind turbines (OWTs), which consists of the lateral *p*-*y* spring, the base moment (M_{base}-θ) spring and the base shear (*T*-*u*) spring. This model is suitable for cases of slender, semi-rigid and rigid piles, and can be modified to include the effects of different soil flow mechanisms, large diameter and base lateral resistances. From the analysis results, the model proposed in this study provides a better prediction and is more appropriate for the design of OWT foundation. The traditional *p*-*y* method underestimates the lateral resistance and stiffness of the soil-pile system, is overly conservative and is not economical for the design of OWT foundations.

Keyword: OWT; Large-diameter monopile; *p*-*y* method; Clay; FE analysis; Soil flow mechanisms

INTRODUCTION

In shallow waters, monopiles are a preferred choice for the foundation of offshore wind turbines (OWTs) due to ease of fabrication and construction (Doherty and Gavin, 2011; Lau, 2015), and accounting for more than 80% of installed wind turbine foundations to date (EWEA, 2016). Considering the harsh ocean environment and the increasing demands for power capacity, the diameters of OWT monopiles have gradually become larger, now commonly between 4 and 8 m (Byrne et al., 2015; Achmus et al., 2019; Wang et al., 2020; Cao et al.,2020). Moreover, the common range of embedded depth of monopile is 25-40 m (Whang et al., 2020), which means that the length to diameter (L_p/D) ratios of monopiles are within the range of 3-8 (Murphy et al., 2018; Wang et al., 2020), this obviously differs from those applied to offshore gas and oil industries. To date, engineers have borrowed the conventional *p-y* method (where *p* is soil resistance per length, in kN/m) recommended by API (2014) and DNV (2018) for the design of large-diameter monopiles in soft clay has still borrowed from offshore gas and oil industries, which is derived from the field tests of small-diameter slender piles, such as the steel-pipe piles with D = 0.324 m and L_p/D = 39.5 (Matlock, 1970). However, increasing evidence shows that the traditional *p-y* method is not appropriate to characterize the behaviors of the large-diameter monopiles with various L_p/D ratios (Kenneth et al., 2012; Lau, 2015; Jung et al., 2015; Byrne et al., 2015,2017; GWEC, 2016; Murphy et al., 2018; Zhang and Andersen,2019; Wang et al., 2020).

On the one hand, there is still discussion about the conclusion that the initial stiffness of the *p-y* spring or the load-displacement curve is directly related to the size of the pile diameter (Ashford and Juirnarongrit, 2005; Fan and Long, 2005; Kim and Jeong, 2011; Finn and

Dowling,2015), which is referred to as the "diameter effect". Furthermore, for a small-diameter pile, the use of the original *p-y* curve can underestimate the stiffness and the ultimate resistance of the test pile (Jeanjean, 2009; Truong and Lehane, 2017; Wang et al., 2020), leading to an inaccurate estimation on the dynamic performance of a wind turbine structure. Thus, the problems mentioned above need to be of great concern in the design of OWTs. On the other hand, the failure mode of a soil-pile system depends on the relative soil-pile stiffness, which is related to L_p/D ratios and soil properties. For a flexible pile (normally having a small diameter and a large slenderness ratio), its failure mode consists of wedge-type flow near the ground surface and full flow below the wedge zone. With a smaller L_p/D ratio (i.e., a more rigid pile-soil system), an additional flow mechanism (a rotational soil flow) near the pile base can be observed (He, 2016; Hong, et al., 2017; Zhang and Andersen,2019; Wang et al., 2020), which differ greatly from the case of a flexible pile. Therefore, the adoption of ultimate soil resistance that is corresponding to the wedge-full-flow failure mechanism is probably not rational for the design of laterally loaded piles. However, there are very few reports about whether rotational soil flow changes the ultimate soil resistance, and it necessitates to be further discussed. Additionally, due to the base movement of semi-rigid and rigid piles, the contributions of the base shear and base moment to the soil resistance become important for the lateral behavior of the soil-monopile system, and it can be gradually enhanced with decreasing L_p/D ratios (Lau, 2015; Byrne et al., 2017; Murphy et al., 2018; Wang et al., 2020). Unfortunately, this point is omitted in the present codes (API, 2014; DNV, 2018).

An OWT is very sensitive to external wind-wave excitations, and the rotation of the pile head is rigorously controlled to ensure the normal operation of a wind turbine. Consequently, a detailed and accurate understanding of soil-pile interaction (SSI) is critical to the safe design of OWT. Given the issues mentioned above, using the conventional *p-y* method for guiding the design of a large-diameter OWT is inadequate, and it is very necessary to improve the original *p-y* approach to adapt the cases of large-diameter monopiles with varied L_p/D ratios. A numerical approach, widely used in practical applications such as the PISA project, is adopted in this paper, and a series of finite element models are established considering pile-soil-water coupling. Based on well-calibrated finite element (FE) models, the soil-pile lateral responses are discussed, then an attempt is made to develop a new unified soil reaction model for the monopiles in clay. This model is suitable for the cases of slender, semi-rigid and rigid piles, and can consider the effect of three soil flow mechanisms, the effect of large diameter and the contributions of base moment and shearing force to the lateral resistance of monopiles.

DESCRIPTION OF THE FE APPROACH

Soil constitutive model

An efficient FEA typically uses the conventional elastic-plastic model for a total stress analysis with a Tresca or a von Mises failure criterion and the modified Cam-clay (MCC) model (Templeton, 2009; Jeanjean, 2009; Jung et al., 2015; Liyanapathirana and Nishanthan, 2016; Yu, 2017; Zhang and Andersen,2019). Whereas the soil-pile interaction under the lateral loads is a complex three-dimensional problem (Peng et al., 2020; Zhou et al., 2020; Luan et al.,2020a,2020b), the potential of FEA for SSI is greatly dependent on the calibration and the choice of soil constitutive model, and whether the constitutive model can accurately capture the non-linear behavior of soil is a key challenge for FEA. Thus, a more advanced and accurate soil constitutive model is recommended for the design of laterally-loaded monopiles in the FE calibration analyse (Byrne et al., 2017; Zdravkovi et al., 2019a). In this paper, a bounding surface soil constitutive model of clay presented by Zhou et al. (2015) is used, which can better predict dilation, softening, shear strain and a steady transition from elastic to plastic behavior of the saturation clay. A simple description on it is introduced in the following:

The formulation of the adopted bounding surface in the p'-q plane is expressed as:

$$F=\left(\frac{q}{Mp'}\right)^{n}+\frac{\ln(p'/p_0)}{\ln(r)} \tag{1}$$

where n and r are the shape parameters of the bounding surface, 1.6 and 2 in the present study, respectively; p_0 is the pre-consolidation pressure; and M denotes the critical state stress ratio.

The initial size of the bounding surface is controlled by p_0. The increment of p_0 is dependent on the plastic volumetric strain and remains consistent with the MCC model. Based on a non-associated flow rule and the condition of consistency, increments of plastic strains are expressed:

$$d\varepsilon_v^p=D_s\Lambda_s=\frac{(M\rho/\bar{\rho})^2-\eta^2}{2\eta}\Lambda_s \tag{2}$$

$$d\varepsilon_s^p=\Lambda_s=\frac{1}{K_p}\left(\frac{\partial F}{\partial p'}dp+\frac{\partial F}{\partial q}dq\right) \tag{3}$$

where Λ_s and D_s are the non-negative loading index and soil dilatancy, respectively; K_p is the plastic modulus; η is the stress ratio, defined as q/p'; ρ and $\bar{\rho}$ represent the distances from the current stress point to the origin point and from the mapping point to origin point, respectively. More details on the constitutive model can be found in Zhou et al. (2015).

Based on the ABAQUS (2006) platform, a UMAT subroutine of the bounding surface plasticity model is developed for computing the responses of the laterally-loaded monopile, which involves 7 material constants and 10 state variables. Meanwhile, considering an easier convergence and computing efficiency for the highly nonlinear problems, the modified Euler integration algorithm (Sloan, 1987) with error control ($TOL < 10^{-5}$ in this paper) is adopted to update the stress at the integration points. To validate the developed subroutine, the undrained monotonic triaxial test of Hyodo et al. (1994) is duplicated. The dimensions of soil specimen are the diameter of 50 mm and the height of 100 mm, the effective mean pressure applied to the sample is 200 kPa. A strain rate of 0.001/min is used in the undrained monotonic triaxial test and the permeability of 1.36×10^{-8} m/s is used here (Liyanapathirana and Nishanthan, 2016). The material parameters of soil are shown in Table 1. From Fig. 1, a good agreement can be observed between the test and the simulation results. In addition, a process of isotropic consolidation is also simulated by using MCC model and UMAT (the bounding surface model). The dimensions of the specimen are 100 mm×100 m×100 m, the effective mean pressure applied to the sample is 100kPa. The material parameters of soil are illustrated in Table 2 (Fei and Peng, 2017). A comparison between the simulation results is shown in Fig. 2 considering different over-consolidation ratios (OCRs). For normal consolidation, the computing curves calculated by UMAT and MCC are coincident. When the over-consolidation ratio is 4, the UMAT result shows a steady transition from elastic to plastic behavior compared to the MCC model result, which is more in accordance with the real behavior of clay.

Table 1 Material properties of Itsukaichi marine clay (Hyodo et al., 1994)

Parameter	Value
A gradient of swelling line κ	0.057
A gradient of virgin consolidation line λ	0.349
Critical state stress ratio M	1.56
Void ratio e_i (p'=1 kPa)	2.632

Initial void ratio e_0	1.837
Poisson's ratio v	0.3

Table 2 Material properties of soil for isotropic consolidation (Fei and Peng, 2017)

Parameter	Value
A gradient of swelling line κ	0.05
A gradient of virgin consolidation line λ	0.15
Critical state stress ratio M	1.2
Void ratio e_i (p'=1 kPa)	2.691
Poisson's ratio v	0.3

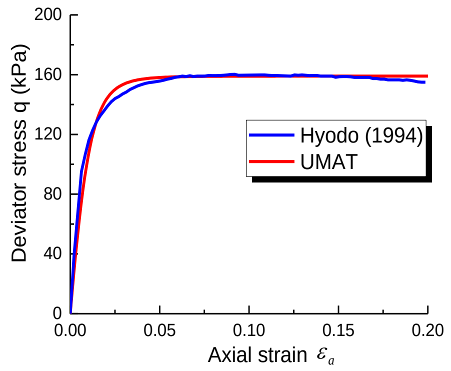

Fig. 1 Comparison between test and simulation results

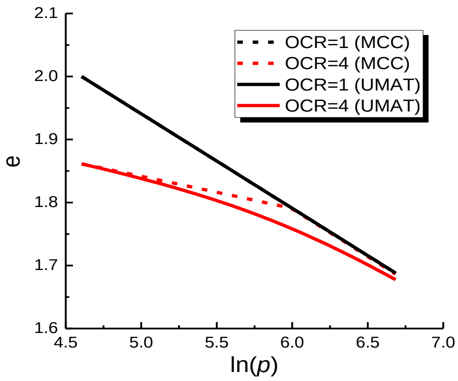

Fig. 2 Curves of *e-ln(p)* for isotropic consolidation

Establishment of FE analytical model

Given the symmetry of the concerned problem, half of the analysis model of each laterally loaded monopile is simulated by the finite element method. The soil is modelled by the solid pore pressure element of C3D8RP with enhanced hourglass control, and the C3D8R element is adopted for monopile. For eliminating the effect of the boundary, the model of the soil is a half-cylinder whose diameter is 20 times the pile diameter. The pinned boundary ($u_x = u_y = u_z = 0$) and lateral constraints ($u_x = u_y = 0$) are used at the base and the lateral cambered surface of the soil container, respectively. Additionally, the displacements of symmetry planes of pile and soil at $Y = 0$ are set to zero (i.e., $u_y = 0$). The meshes located in the shallow layer and near the pile are dense, and the pile mesh below the mudline is consistent with soil mesh, where the amount of mesh along the pile thickness is more than 6 to ensure the calculation accuracy of the internal forces on the pile shaft. Convergence analysis of the mesh is performed for all FE models in this paper, and a typical FE mesh used is illustrated in Fig. 3. Surface-to-surface contact behavior is adopted to model the pile-soil interaction, which is a combination of the Coulomb friction law and hard contact considering separation after contact. The friction coefficient of the soil-pile (clay-steel) interface is 0.3 calculated by the formulation recommended by Randolph (1981). The pile top is free and its load is applied by a Coupling Constraint.

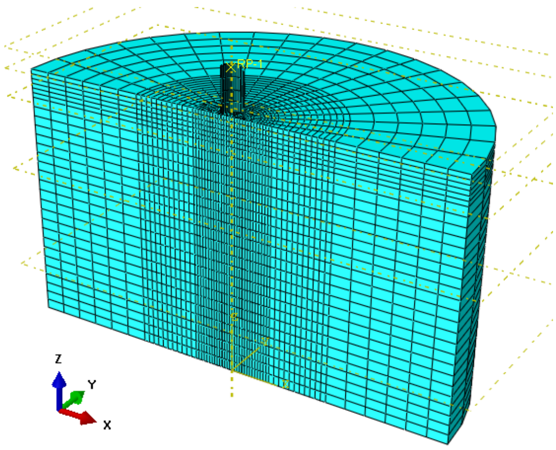

Fig. 3 Typical FE mesh used in SSI analysis

The initial geostatic stress field caused by the soil self-weight has an important influence on the pile-soil contact behavior and the size of the initial yield surface of soil. Consequently, the equilibrium of the initial geostress field is critical to the subsequent geotechnical analysis. In the present study, the whole analysis programme consists of a geostatic analysis step for the initial conditions of the soil container, a static analysis step for loading gravity of the monopile, and a pile-soil-water coupling analysis step (undrained analysis by Soils Step) for calculating the lateral responses of the soil-pile system, where the undrained analysis is carried out based on excess pore pressures and all external boundaries of the soil container are undrained. Kaolin clay is adopted for the soil container of all FE models, and its material parameters are shown in Table 3. The non-uniform distributions of initial void ratio e_0, over-consolidation ratio and elastic modulus E_s within the soil can be defined by the UMAT subroutine (see Eq. (4)). Steel pipe monopile is regarded as an isotropic hardening elastic-plastic material with the Mises failure criterion, and the fundamental material parameters of steel are also displayed in Table 3.

$$E_s = 3(1-2v)\frac{(1+e)p'}{\kappa} \tag{4}$$

Where κ is the slope of the swelling line; v is a constant Poisson's ratio; and e is the void ratio.

Table 3 Summary of material properties for SSI analysis in this study

Material	Parameter	Value	Remark
Kaolin clay	A gradient of swelling line κ	0.05	Jeanjean (2009)
	A gradient of virgin consolidation line λ	0.25	
	Lateral earth pressure coefficient at rest K_0	0.64	
	Critical state stress ratio M	0.8	
	Void ratio e_i (p'=1 kPa)	3.58	
	Special gravity Gs	2.64	
	Poisson's ratio v	0.3	
	Permeability k (m/s)	1×10^{-9}	He (2016)
	Friction angle φ (degrees)	22	He (2016) and Lehane (2009)
Steel pile	Elastic modulus E_p (Gpa)	206	

Poisson's ratio v	0.3	Jeanjean (2009)
Density (kg/m^3)	7800	
Yield strength (MPa)	414	
Yield ratio	1.3	

Verification of the FE model

The verification of the FE analytical model is performed using the centrifuge test results reported by Jeanjean (2009). The scale factor of the centrifuge test was 1:48, the free-head test pile had the prototype outside diameter of 0.91 m and the wall thickness of 50.8 mm, the embedded prototype length of the single pile was 20.2 m, and the eccentricity of 4.3 m above the mudline. The soil used in the test is fine Alwhile Kaolin Clay and designed to be slightly over-consolidation with depth. Its material properties are illustrated in Table 3. In this paper, the FE model of the centrifuge test is modelled on the basis of the approach mentioned above. The shear strength profile from a PCPT test is illustrated in Fig. 5, and the fitting formulation of the strength ratio with OCR is displayed as follow (Jeanjean, 2009):

$$\frac{s_u}{\sigma_v'} = 0.19(OCR)^{0.67} \tag{5}$$

where s_u and σ_v' are the shear strength and the effective vertical stress of the soil, respectively.

For an accurate capture of the behavior of the kaolin clay, the distribution of OCR is considered along the depth. The approximate OCR profile (see Fig. 4(b)) can be obtained from a back-calculation according to Eq. (5) and the undrained shear strength profile is shown in the Fig. 4(a). Note that a sharp increase in the PCPT profile locates approximately 11m below the ground surface due to the existence of a thin drain sand layer in the centrifuge test, and the sand layer is excluded in the prototype FE analysis herein. In Fig. 4(a), the s_u used in the FE analysis of Jeanjean (2009) (the blue one) obviously differs from the test result at the mudline, thus the shear strength profile in black is used for the current study. In addition, a profile of undrained shear strength based on the critical state soil mechanics (CSSM) theory, referred to as Eq. (6) (Wroth, 1984), is also shown in the figure (the orange one). This provide a method for predicting the undrained shear strength of soil below a depth of 20.2 m. Good agreement can be seen between the test results and CSSM theory results.

$$\frac{s_u}{p'} = \frac{M}{2}\left(\frac{OCR}{r}\right)^{\frac{\lambda-\kappa}{\lambda}} \tag{6}$$

where p' is the current effective mean pressure of soil; r is a constant and corresponds to Eq. (1).

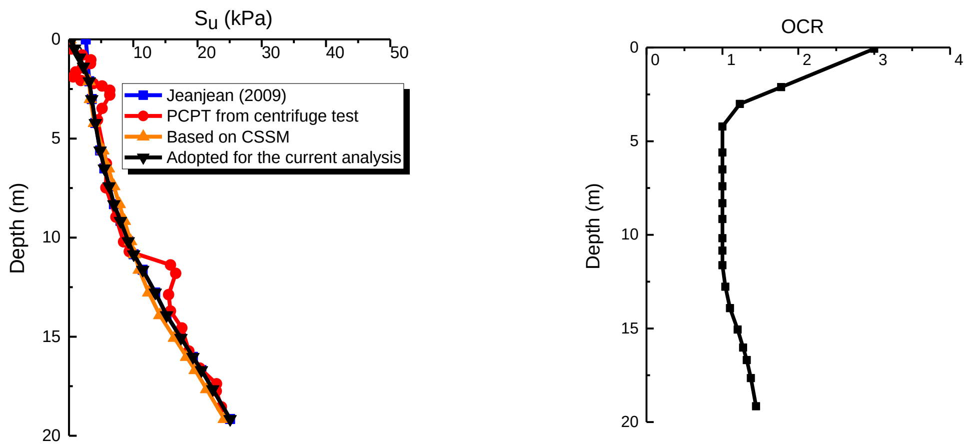

(a) Undrained shear strength s_u (b) OCR from the back-analysis

Fig. 4 Profiles of soil parameters

The monotonic lateral loading test is simulated on the basis of the developed FE model. In the post-processing module of the software, the section shear force and the moment can be outputted by establishing a series of slices, and the central finite difference technique is used to obtain the relationship between unit soil pressure (P in kPa) and lateral displacement (y). The curves of the normalized soil pressure (P/s_u) against the normalized deflection (y/D) are illustrated in Fig. 5. From the comparison of *P*-*y* curves from the different data sources for different depths, we know that the results of this paper are closer to the test results in the terms of the trend and the magnitude, more exact than those from the FEA of Jeanjean (2009) as well as the API's *P*-*y* curves that obviously deviate from the test results. Furthermore, the profiles of the ultimate resistance coefficient N_p (i.e., P/s_u corresponding to y/D of 0.2) above the depth of z/D = 12 are shown in Fig. 6. The N_p from the current FE model and the one from the FEA of Jeanjean (2009) are basically consistent with the result of the centrifuge test, but the results of the present study have a more obviously regular, i.e., an increasing N_p in the shallow layer and a steady N_p in the lower layer, which corresponds to widely accepted results. Additionally, a similar centrifuge test on the lateral loaded pile in Kaolin clay was also performed by Guo et al. (2014) and the CPT-based N_p profile is depicted in Fig. 6. A good match can be observed when *z/D* is more than 3. In short, the FE model in the paper is validated.

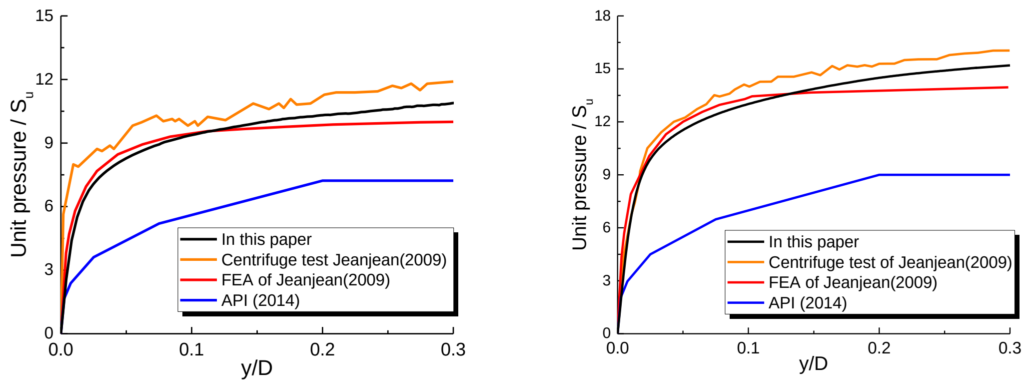

(a) Depth = 1.5*D*　　　　(b) Depth = 9*D*

Fig. 5 Comparison of *P*-*y* curves at different depths

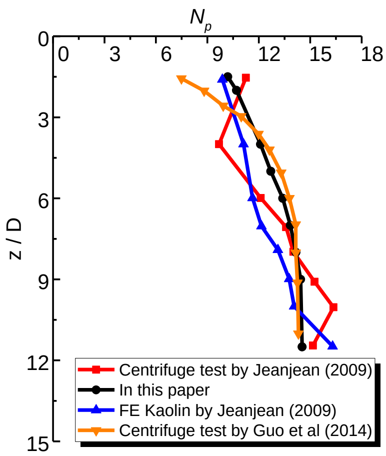

Fig. 6 Comparison of the ultimate resistance coefficient N_p

SOIL-PILE RESPONSES ANALYSIS AND DEVELOPMENT OF THE SOIL REACTION MODEL

The numerical study is conducted by using three-dimensional finite element models established on the basis of the previously mentioned approach. For the subsequently discussed piles, the wall thickness of each monopile is 1.10% of the diameter. Additionally, the material properties of the soil layer keep the same as Table 3, but the OCR below the depth of 20.2 m is the same as that at the depth of 20.2 m. The relative stiffness factor (K_r) of the pile-soil system is calculated by $\frac{E_p I_p}{E_{s,avg} L_p^4}$ (where $E_{s,avg}$ is the average Young's modulus of soil within the embedded length), and the soil-pile rigidity is identified on the basis of the criterion of Poulos and Hull (1989) (i.e., the upper bound and lower bound of K_r for rigid and flexible piles are 0.208 and 0.0025, respectively). The programme for the numerical study is displayed in Table 4.

Table 4 Programme for numerical parametric study

Pile diameter D (m)	Embedded length L_p (m)	L_p/D ratio	Relative stiffness factor (K_r)	Pile rigidity
0.91	20.2	22.2	9.9×10^{-4}	Flexible

2	20.2	10.1	0.023	Semi-rigid
4.04	20.2	5.0	0.385	Rigid
6	20.2	3.37	1.874	Rigid
6	30	5	0.270	Rigid
8	40	5	0.208	Rigid

Soil flow mechanisms

The displacement contours and vector fields are shown in Fig. 7, where only the models with L_p = 20.2 m are displayed and the constant-length arrows are used in the vector field for convenience. Under the lateral load, surface soil in the front of the pile is distinctly lifted and the gap at the back of the pile forms. For the case of a flexible pile (see Fig. 7(a)), the external load on the pile head is mainly resisted by the soil within the depth of 7D, the lower soil layer doesn't almost participate in sharing the load; meanwhile, an obvious soil-pile gap and no base displacement can be observed. However, with the reduction of L_p/D (a greater K_r), the resistance of the pile is provided by more soil, and the gap between the soil and the pile further develops and reaches at the deeper stratum in Figs. 7(b)-(d). In addition, a clear toe-kick and a gap at the base pile can be observed, which means that the base shear exists a contribution to the lateral resistance of the pile. It is worth noting that the gap at the shallow layer can close when the pile diameter is more than 4.04 m, it is because that the large self-weight leads to a considerable shear slip of the soil.

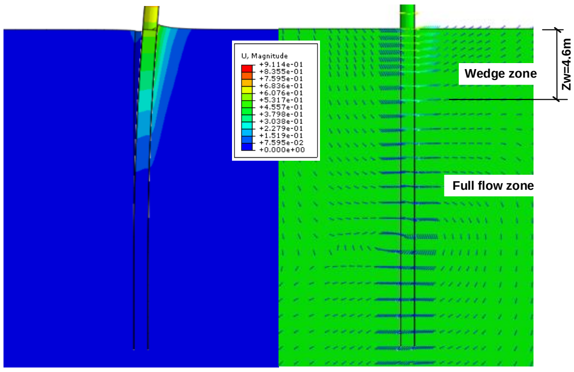

(a) D = 0.91 m, L_p = 20.2 m, K_r = 9.9×10^{-4}

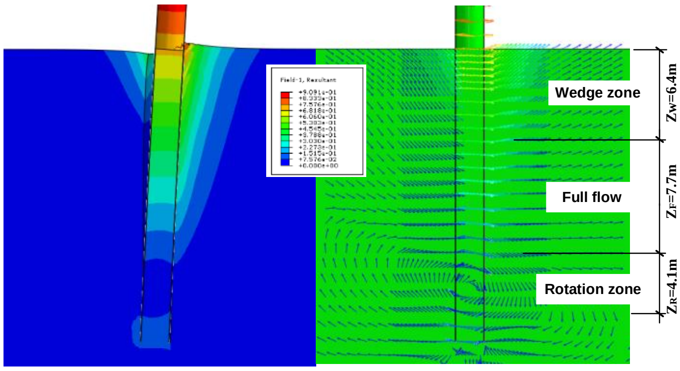

(b) D = 2 m, L_p = 20.2 m, K_r = 0.023

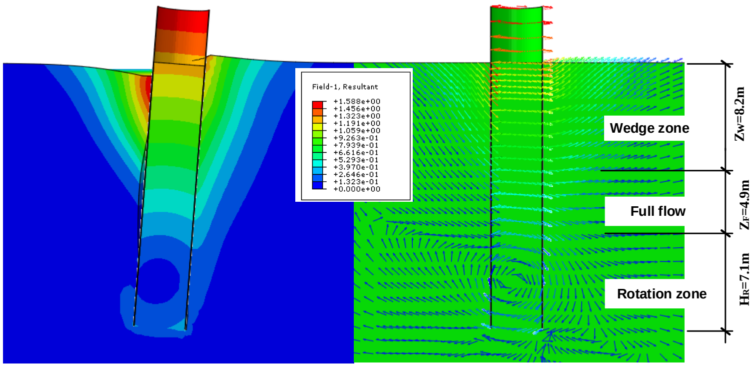

(c) D = 4.04 m, L_p = 20.2 m, K_r = 0.385

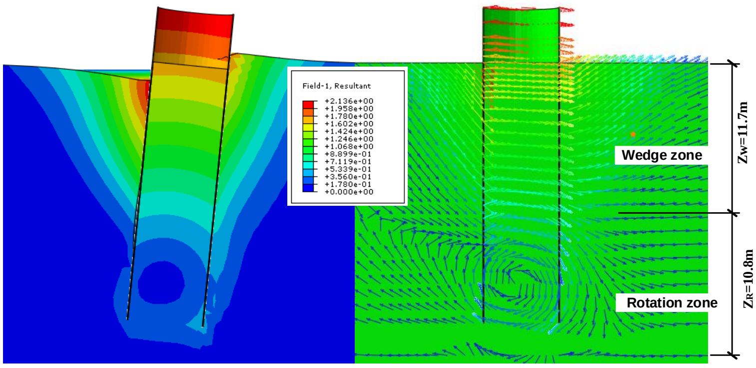

(d) D = 6 m, L_p = 20.2 m, K_r = 1.874

Fig. 7 Contours and vector fields of soil displacement

For the small diameter pile in Fig. 7(a), the soil flow mechanism only consists of an upper wedge-type flow and a full flow being below the wedge-type zone (all vector fields are displayed on an undeformed mesh herein), which is also widely accepted and used in the pile design by API (2014). While the large diameter pile increases, referring to Figs. 7(b)-(d), the monopile clearly rotates around a certain point of the pile shaft, and an entirely different soil flow mode can be observed. The flow mode located near the pile toe is termed as a rotational soil flow. Meanwhile, its influenced area gradually enlarges with a smaller L_p/D, especially because only wedge-type flow and rotational flow can be observed in the case of L_p/D = 3.37. Moreover, the height of wedge failure is also relative to the pile diameter. This implies that the flow mechanism significantly changes with pile diameters and L_p/D ratios, which is bound to influence the soil-pile lateral behavior, but this point is ignored in the conventional *p-y* method and should be considered.

Depth of the rotation point

Fig. 8 shows the dimensionless profiles of normalized pile deflection (y/D. versus. z/L_p) when the lateral displacement at the mudline, y_m, is 0.2D. For the slender pile (a black solid line), its profile behaves as a bending deformation. With regard to the semi-rigid pile of L_p/D = 10.1, it not only bends but also rotates around the point lying at 0.81L_p. With the further reduction of L_p/D, the pile motion turns into a pure rigid-body rotation and the location of the rotation point, z_{RP}, is slightly below 0.81L_p. From Fig. 9, the dimensionless depth of rotation point for the semi-rigid or the rigid pile shifts downwards with an increase of y_m, gradually tending to converge. The converge values of z_{RP}/L_p are rather close to one other, and its range is 0.81L_p-0.85L_p and consistent with some reported results (Lau, 2015; He, 2016; Truong and

Lehane, 2017; Murphy et al., 2018; Wang et al., 2020). In addition, the position of rotation the point almost becomes lower when the pile diameter augments, as shown in Fig. 9, and the fitting relationship of z_R/L_p with D is illustrated in Fig. 10.

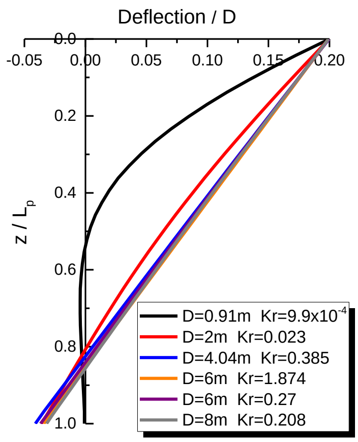

Fig. 8 Profile of the normalized deflection

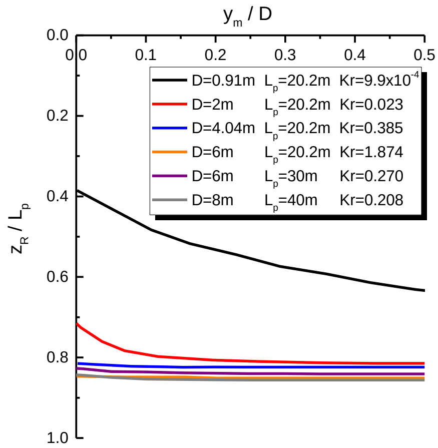

Fig. 9 Change of the normalized depth of rotation point with y_m/D

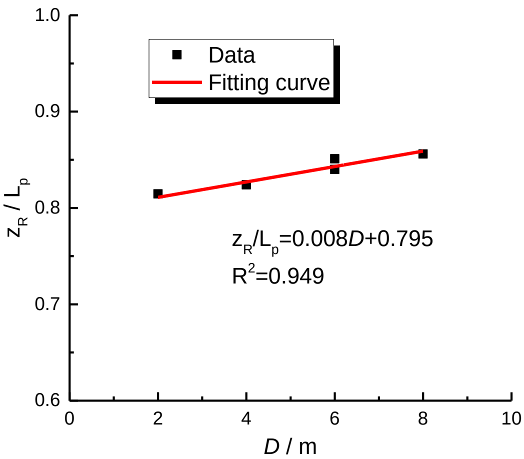

Fig. 10 Variation of z_{RP}/L_p with D

Ultimate unit soil pressure (P_u)

As shown previously, the diversities of the pile-soil motion and the flow mode exists between the different pile diameters, which may influence the ultimate soil resistance. Similarly, this point is also mentioned in several reports (Lau, 2015; He, 2015; Hong et al., 2017). However, it is seldom considered in *p*-*y* curves, especially for those of large diameter monopile. Thus, this issue is necessary to be discussed in detail in the subsection.

The lateral displacement of some measured slices near the rotation point cannot reach the failure criterion of y = 0.2D due to the rotation of the pile shaft. For an illustration, the normalized *P-y* curves are shown in Fig. 11 and a similar curve shape can be found for each slice at different depths regardless of the difference of their lateral displacement. Given the similarity of the *p-y* curve for every segment of the pile (Jeanjean, 2009; Truong and Lehane, 2017), the N_p of these slices are obtained from fitting functions such as hyperbolic tangent function (Jeanjean, 2009; Truong and Lehane, 2017) or hyperbolic function (Georgiadis et al., 1992) (meeting the premise of variance $R^2 \geq 0.99$). A similar method can also be found in Tzivakos and Kavvadas (2014). The profiles of the ultimate resistance coefficient for all cases are displayed in Fig.12 and those points from the fitting function are signed by a hollow scatter point in the graphs.

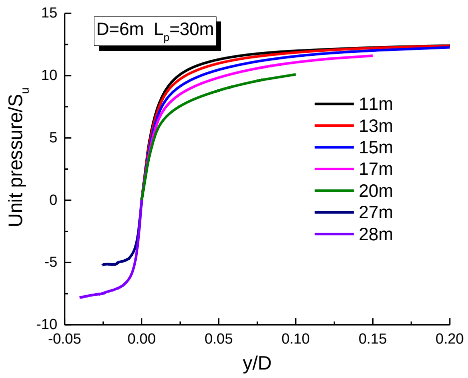

Fig. 11 Normalized *P-y* curves from FEA (D = 6 m, L_p = 30 m)

For the pile of 0.91 m in diameter (a flexible pile) in Fig. 12(a), the computed N_p increases with depth in the shallow layer and basically remains a constant in the lower stratum. The profile is also similar to those recommended by API (2014) and DNV (2018). However, when the pile diameter augments (a semi-rigid or rigid pile), the N_p profile changes noticeably. Except that the locus at the upper half of the shaft is similar to one of D = 0.91 m, the values of N_p

clearly decrease in the lower half of pile length, then its absolute value gradually increases below the position of rotation, and the track of N_p of the lower half part is very similar to a locus of the hyperbolic tangent function. Additionally, when K_r is equal to 1.874 (i.e., D = 6 m, L_p = 20.2 m), the constant piece of N_p profile is hardly observable, which is consistent with Fig. 7 described previously. From Fig. 12(b), we know that the effect of pile length on the N_p magnitude in the upper half zone and the location of the wedge-full-flow transition is insignificant; this phenomenon is corresponding to the description of Murff and Hamilton (1993). Noting that a change in the pile length will lead to a change of relative soil-pile stiffness, this may imply the value of N_p is independent of K_r. To further investigate the N_p of large diameter pile, three different diameters are discussed when L_p/D = 5 (of course, they are rigid piles), and the computed results of the ultimate resistance coefficient are shown in Fig. 12(c). It can be clearly observed that N_p decreases with increasing pile diameter; this point is also proven by Fig. 12(a), therein, the maximum N_p of D = 8 m decreases nearly 15% compared to that of D = 0.91 m. In addition, since the zone height of each flow mode in the soil container will change with pile diameter, bringing about the difference of shape of N_p profile, the phenomenon that N_p is relative to pile diameter is also reported by He (2015), however, it is seldom taken into account in the current *p*-*y* method for large diameter monopiles. The range of computed maximum $N_{p,\,max}$ (defined as N_p located in the full flow zone) is from 12.1 to 14.2 from the FEA results, obviously larger than 9 (Matlock, 1970) and 9-11.94 from the theoretical solutions (Murff and Hamilton, 1993; Yu et al., 2015). Nevertheless, the range of $N_{p,\,max}$ computed herein is close to those of 12-16 from the centrifuge tests (Jeanjean, 2009; Guo et al., 2014; Truong and Lehane, 2017) and the numerical analysis (Jeanjean, 2009; Templeton, 2009;

Tzivakos and Kavvadas, 2014). This is a probable reason that the operational undrained strength (s_u from the PCPT test is adopted in the paper) is used to calculate the value of N_p in the current study. Truong and Lehane (2017) have particularly discussed the difference in the evaluation of N_p due to using s_u from various sources.

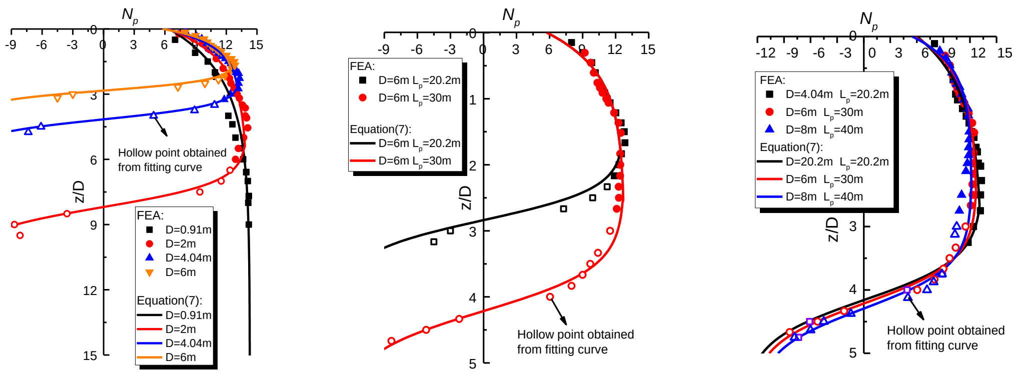

(a) Different diameter (b) Different length (c) Same L_p/D ratio

Fig. 12 Profiles of ultimate resistance coefficient for all cases

To consider the effects of the pile diameter and the rotational soil flow on the ultimate soil resistance, empirical formulations for calculating P_u are provided in Eqs. (7)-(11), which differs from the one originating from the wedge-full-flow failure of the small-diameter slender pile. The developed formulations include the effects of the rotational soil flow and the pile diameter, which can be applied to a flexible pile, but also a semi-rigid or rigid pile (just for a flexible pile, only the upper part of Eq. (8) is used).

$$P_u = N_p s_u \tag{7}$$

$$N_p = \delta \begin{cases} N_{p,\max}(1-0.55e^{-\zeta z/D}) & z < z_{RP} - h_R \\ N_{p,\max}\tanh(\alpha \dfrac{z_{RP}-z}{D}) & z_{RP} - h_R \le z < L_p \end{cases} \tag{8}$$

$$\frac{N_{p,\max}}{N_{p,\max}^{ref}} = -0.019\frac{D}{D_{ref}} + 1.026 \tag{9}$$

$$\zeta = 0.22\frac{D}{D_{ref}} + \frac{s_{u1}}{\gamma'} \tag{10}$$

$$\alpha = 5.45\left(\frac{L_p}{D}\right)^{-0.79} \tag{11}$$

where δ is a correction factor related to the source of s_u and discussed in the following; z is the depth of a given point; ζ and α are two fitting coefficients, calculated from the Eqs. (10)-(11); D_{ref} and $N_{p,max}^{ref}$ are a reference diameter and an ultimate resistance coefficient at the full flow zone for the case corresponding to the reference diameter, respectively, 0.91 m and 14.2 for this paper; s_{u1} denotes the gradient of undrained shear strength with depth, as taken to 1.25 kPa/m in the current study (Jeanjean, 2009); z_{RP} is the depth of the rotation point and approximately determined by the Fig. 10; and h_R is the influence radius of rotational flow soil, and it can be obtained by setting the upper and lower parts of Eq. (8) to be equal.

For the soil of the same site, the undrained shear strengths measured by different test methods cause different deviations from the actual in-situ value; thus, the value of N_p is different based on different measuring methods, that is, the p-y curves are related to test parameters (Anderson et al., 2003; Guo et al., 2014; Truong and Lehane, 2017). Out of consideration for this, the correction factor δ is used herein to adapt the difference of the value of N_p due to the different measurement approaches. The value of δ can be approximately obtained from an empirical relationship of different test sources of s_u. It is noted that both the T-bar test and the CPT test were performed in the centrifuge test of laterally loaded pile reported by Truong and Lehane (2017), and 1.4z kPa of undrained strength ($s_{u,T\text{-}bar}$) from the T-bar test and 19.6z kPa of cone net resistance (q_{net}) from CPT test is measured when the OCR is 1 (Truong and Lehane (2017) and Guo et al. (2014)). Given the dimensionless cone factor N_c, which is typically 10-17 for cohesive soil (Yu and Houlsby, 1990; Teh and Houlsby, 1991), the value of the correction factor δ is inferred from the ratio of $s_{u,T\text{-}bar}$ to (q_{net}/N_c). The correction factors relating to the test sources are illustrated in Table 5.

Table 5 Approximate value for correction factor δ from back analysis

Source of s_u	Value of δ	Remarks
CPT	1.0	
T-bar	0.93	Derived from results of Truong and Lehane (2017) and Guo et al. (2014), and N_c=15 (Damgaard et al., 2014)
UU	1.14	Derived from $s_{u,UU}$=0.7$s_{u,CU}$ reported by Chen and Kulhawy (1993)
CU	0.80	Derived from $s_{u,CU}$=1.17$s_{u,T\text{-}bar}$ reported by Truong and Lehane (2017)

Good agreement is shown between the results for N_p from the fitting equations and those from the 3D FEA; as shown in Fig.12, the proposed formulas can reflect on the effect of pile diameter and rotational soil flow on the ultimate soil pressure. Furthermore, a comparison between the results from Eqs. (7)-(11) and the centrifuge test (Truong and Lehane, 2017) is also conducted for verification. The prototype of the test pile was 0.88 m in diameter and 10.56 m in length, the soil used was kaolin clay and its undrained shear strength profile was measured by the T-bar test. More details can be found in Lehane et al. (2009) and Truong and Lehane (2017). A satisfying match can also be seen in Fig. 13, and the reliability of the developed equations is validated.

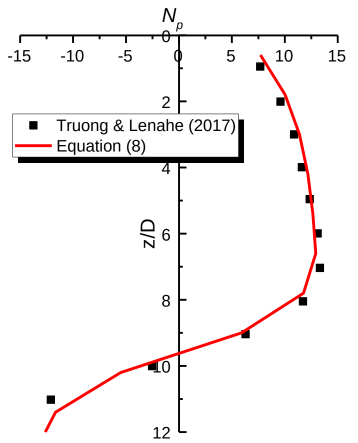

Fig. 13 Comparison of result in this paper and that from Truong and Lehane (2017)

Characterizing the *p-y* curve

Based on the computed *p-y* curves extracted via the three-dimensional FE models, a unified *p-y* model that can characterize the effect of different diameters and soil flow mechanisms on the ultimate soil resistance is proposed in the present study. Fig. 14 gives a comparison between the *p-y* curves from FEA. The lateral soil resistance, *p*, is normalized by $P_u D$, while the lateral displacement, *y*, is normalized by *D*. From these figures, the *p-y* curves at the different depths of each pile are like each other. In addition, when the embedded length of the pile remains constant, as seen in Fig. 14(a), a higher initial stiffness and earlier ultimate resistance can be found with an increasing pile diameter, which corresponds the conclusions from Wang et al. (2020). However, when not keeping the embedded length constant, we can found that the stiffness of the *p-y* curve is controlled by the length-to-diameter ratio. On the one hand, although the diameters are different in Fig. 14(c), their *p-y* curves at different depths are very similar overall when the length-to-diameter ratios are all equal to 5; on the other hand, the case of L_p = 20.2 m has a higher initial stiffness than that of L_p = 30 m when the diameter is 6m in Fig. 14(b). In fact, as far as Fig. 14(a) is concerned, a changing diameter means a varied L_p/D

ratio when the pile length is unchanged. Thus, the stiffness of the *p*-*y* curve is still related to the ratio of length to diameter. Detail needs to be noted that Wang et al. (2020) drew that the stiffness of the *p*-*y* curve was related to pile diameter, but his investigation was based on the same embedded length (L_p = 30 m). In other words, the stiffness of the *p*-*y* curves is related to the L_p/D ratio rather than the pile diameter. The findings can also be supported by Fig. 15, which suggests that the elastic stiffness of the *p*-*y* spring is significantly related to the L_p/D ratio, i.e., the smaller L_p/D ratio and the larger initial stiffness. It also implies that the *p*-*y* curves originating from the field tests of L_p/D = 39.5 (Matlock, 1970) raise questions about the extending monopile design of OWTs.

An attempt is carried out to fit the computed *p*-*y* curves by a hyperbolic tangent function which is typically adopted for the fitting *p*-*y* curve. As shown in Fig. 14 and Eqs. (12)-(13), we can see that the developed empirical equations have a good matching with results of FEA and can indicate the variation of the stiffness of the *p*-*y* spring with L_p/D ratio. Furtherly, a comparison between *p*-*y* curves at z = 10 m is also given in Fig. 16. Different from the good agreement between the FEA and the proposed formulation, the API (2014) curves obviously have a lower ultimate soil resistance and a softer stiffness than those simulated in this study. Consequently, it is necessitated the development of a new *p*-*y* method for better depicting the soil-pile behavior.

$$\frac{p}{P_u D} = \tanh\left(a\left(\frac{y}{D}\right)^{0.5}\right) \tag{12}$$

$$a = 8.62\left(\frac{L_p}{D}\right)^{-0.18} \tag{13}$$

where P_u is the ultimate unit soil pressure at a given depth; y is a lateral displacement of the pile shaft at a given depth; and a is an empirical coefficient related to the length-to-diameter ratio and can be determined by Eq. (13).

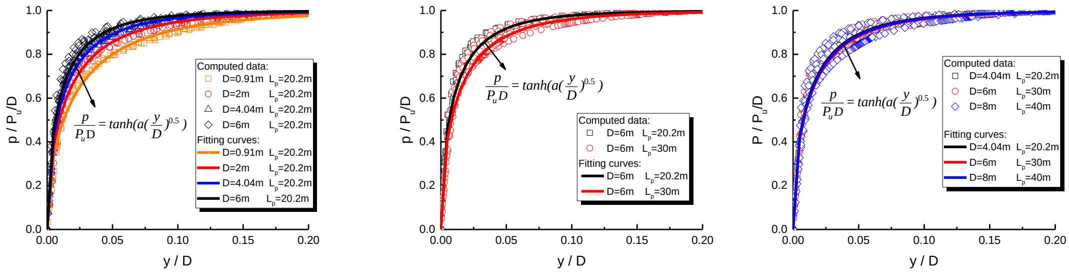

(a) Different diameter (b) Different length (c) Same L_p/D ratio

Fig. 14 Comparison between *p*-*y* curves from FEA and ones fitted by function

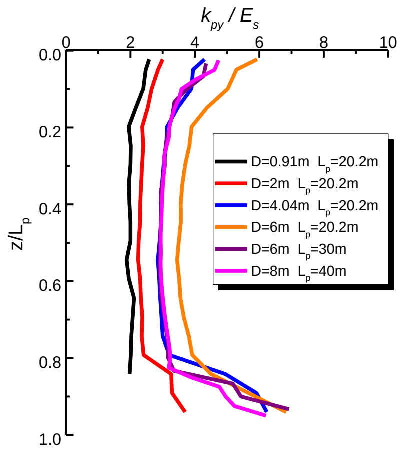

Fig. 15 Normalized *p*-*y* initial stiffness (k_{py}/E_s)

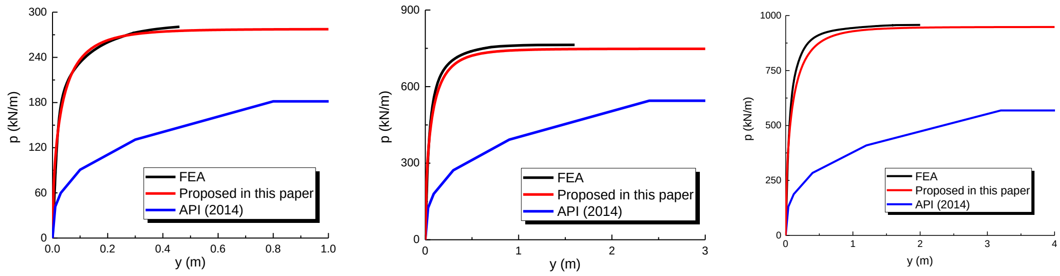

(a) D = 2 m, L_p = 20.2 m (b) D = 6 m, L_p = 20.2 m (c) D=8 m, L_p = 40 m

Fig. 16 Comparison of *p*-*y* curves at z = 10 m

Shear force and moment of pile base

For understanding the contributions of different resistance components to the lateral resistance of a large-diameter monopile, pushover analyses considering the different resistance components are carried out while the pile is D = 6 m and L_p = 20.2 m. As shown in tFig. 17, both the shear force and the moment at the pile toe are a significant influence on the lateral resistance of the large diameter pile, and their total contribution is nearly 23.5%, 11.2% from the base moment and 12.3% from the base shear, similar to the investigations of Murphy et al. (2018) and Wang et al. (2020). Therefore, only the lateral resistance from the soil around the pile for the foundation design of OWT is over-conservative and not economical, the contribution from pile toe resistance must be considered in the present *p*-*y* method for more accurately capturing soil-pile behavior.

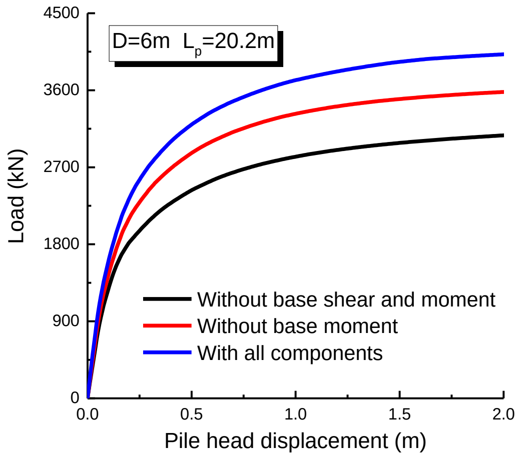

Fig. 17 Pushover analyses considering different resistance components

Figs. 18-19 give the base shear forces and moments for all cases. For a small-diameter slender pile, the base moment is not displayed due to its very small values, which also implies that the base shear and moment for a slender pile can be ignored (this point will also be included below). Nevertheless, when the pile is more rigid with increasing diameter, the shear force and the base moment at the pile base become sharply large. Considering the aim mentioned above, two soil springs, the base moment (M_{base}-θ) spring and the base shear (T-u) one, are proposed herein. The empirical equations are developed and see Eqs. (14)-(17).

$$\frac{T}{T_u} = \tanh(7.33(\frac{u}{D})^{0.55}) \quad (14)$$

$$\frac{T_u}{D^2 s_{u,base}} = (0.15D^{1.49} + \frac{14.56}{D}) \quad (15)$$

where u is the lateral displacement of the pile base; $s_{u,base}$ is the undrained strength of the soil placed at the pile base; and T and T_u are the shear force and the ultimate force at the pile toe, respectively.

$$\frac{M_{base}}{\mathrm{M}_{base,u}} = \tanh(6.1\theta^{0.51}) \quad (16)$$

$$\frac{M_{base,u}}{DL_p^2 s_{u,base}} = 0.039K_r + 0.036 \quad (17)$$

where M_{base} and $M_{base,u}$ are the moment and the ultimate moment at the pile toe , respectively; θ is the rotation angle of the pile toe, equal to the first-order differential of lateral displacement versus height; and K_r is the soil-pile relative stiffness mentioned above.

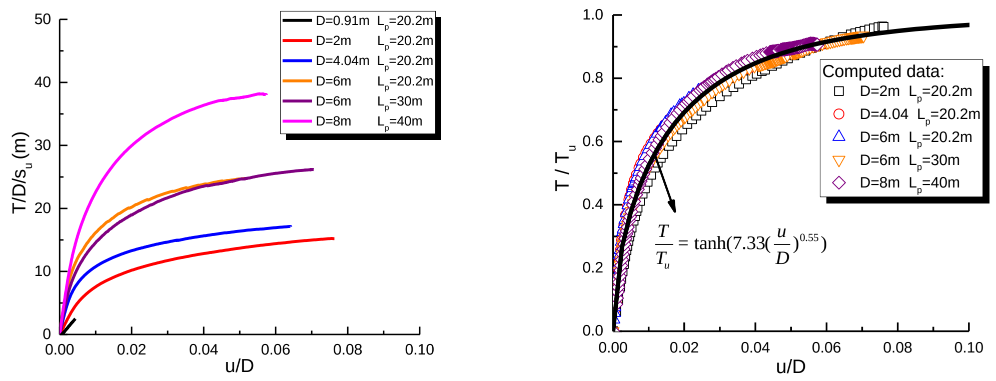

(a) (b)

Fig. 18 Relationship between base shear force and lateral displacement

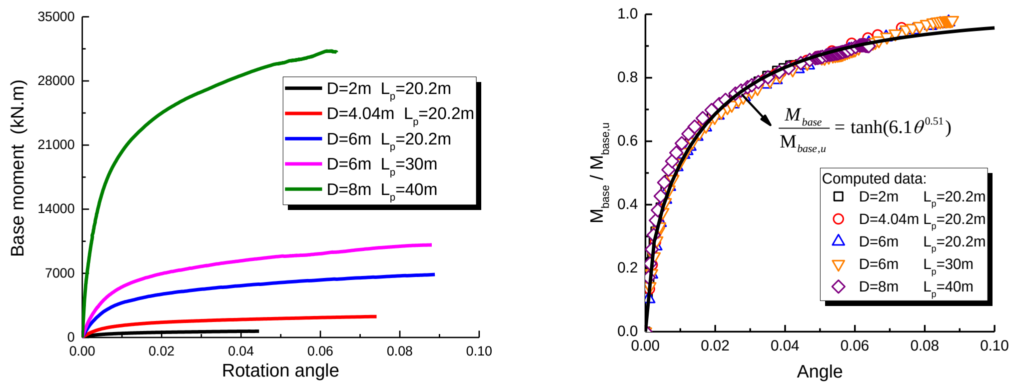

(a) (b)

Fig. 19 Relationship between base moment and rotation angle

To verify the quality of the proposed soil reaction model in the paper, a comparison between the load-displacement curves of three typical piles (flexible, semi-rigid and rigid piles) is performed, as illustrated in Fig. 20. It should be explained that the non-black solid curves in Fig. 20 are obtained from the pushover analyses of soil-pile FE models that use soil resistance springs instead of the real soil layer. Considering that the distributional moment caused by the vertical shear stress along the pile shaft contributes to the lateral resistance (Byrne et al, 2015., 2017; Murphy et al.,2018; Wang et al., 2020), the *t-z* curve recommended by the API (2014) is used in all FE models with soil springs. Additionally, to be more consistent with the real condition of monopiles, the *Q-z* curve recommended by the API (2014) is also used in all FE models with soil springs. From Fig. 20, the proposed soil reaction model has a good match with the computed results from 3D FEA for three typical piles. And the use of API (2014)'s *p-y* method obviously underestimates the lateral stiffness and the ultimate lateral resistance compared to the computed results from 3D FEA, particularly an underestimation of nearly 150% of the stiffness and the ultimate capacity for a rigid pile.

For a flexible pile, the shear force and moment at the pile toe are insignificant, which suggests that the adoption of only a lateral *p-y* spring is sufficiently accurate for describing pile lateral performance. However, with pile diameter and K_r augmenting, the contribution of the additional resistances from the pile toe is more profound, and the consideration of only the *p-y* spring increasingly deviates from the actual load-displacement curves, which leads to a clear underestimation. As a consequence, the consideration of the base moment and the base shear force is very necessary for a large-diameter rigid monopile widely adopted in the OWT industry.

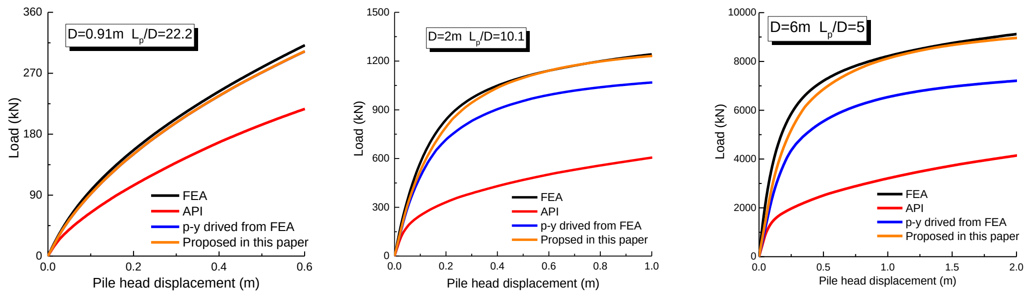

(a) Flexible pile (b) Semi-rigid pile (c) Rigid pile

Fig. 20 Comparison between load-displacement curves of three typical piles

INFLUENCE OF THE ROTATIONAL SOIL FLOW ON THE ESTIMATION OF LATERAL BEHAVIOR

To further reinforce the concept that the rotational soil flow has an important influence on the evaluation of soil-pile lateral behavior, the N_p profile derives from the wedge-full-flow failure mechanism and the one derived from the wedge-full-flow-rotation failure mechanism are used, respectively, to predict the load-displacement curve of the pile. Fig. 21 illustrates a comparison of the load-displacement curves of a large-diameter monopile with D = 6 m and L_p/D = 5 considering different soil flow mechanisms. From Fig. 21, we can know that the rotational soil flow has an obvious influence on the estimation of the ultimate lateral resistance, and it overestimates the ultimate lateral bearing capacity of the pile if ignoring the additional flow soil mode. As a result, using a traditional *p-y* method based on the wedge-full-flow failure mechanism is not conservative for the design of a large-diameter monopile of an OWT.

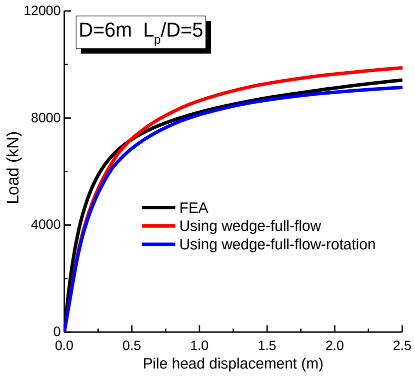

Fig. 21 Comparison of load-displacement curves

VERIFICATION OF THE DEVELOPED SOIL REACTION MODEL

The purpose of this section is to verify the prediction capability of the developed soil reaction model against published monopile results obtained from field and centrifuge tests. To be consistent with offshore foundations, two short piles with a small slenderness ratio in clay are chosen, i.e., L_p/D = 12 from the centrifuge test (Truong and Lehane,2017) and 5.18 from the field test of the PISA project (Zdravkovi et al.,2019; Byrne et al., 2019). The basic geometric information about the two test piles is summarized in Table 6. The performance of the proposed model is shown in the following subsections. Of course, comparisons of the results of the model with that of the *p-y* model recommended by the API (2014) are also carried out.

Table 6 Parameters of test piles for validation

Pile information	Centrifuge test (Truong and Lehane,2017)	PISA field test (Zdravkovi et al.,2019; Byrne et al., 2019)
Diameter (m)	0.88	2
Embedded length (m)	10.56	10.35

Wall thickness (mm)	80	25
Eccentricity (m)	1.36	10.1
Length to diameter ratio	12	5.18

Centrifuge test

Truong and Lehane (2017) reported centrifuge tests on a series of laterally loaded monopiles in Kaolin clay considering different pile shapes and OCRs. A circular open pile in normal consolidation clay is used for a validation analysis here, whose flexural rigidity *EI* of prototype pile is 1×10^6 kN.m^2, an efficient weight of 6kN/m^3 and an approximate 1.4 kPa/m of the gradient of undrained strength from the T-bar test (Truong and Lehane, 2017). Fig. 22 illustrates the measured normalized load-displacement response of the test pile, and the predicted result from the proposed model as well as that from the API (2014)'s *p-y* model. A very small difference can be seen when the predicted result compares with the measured one, which means that the developed soil reaction model in the paper can precisely capture the lateral behavior of the test pile. As to the load-displacement curve calculated by the API (2014), it obviously underestimates the ultimate resistance of the test pile (nearly -40%) and is over-conservative.

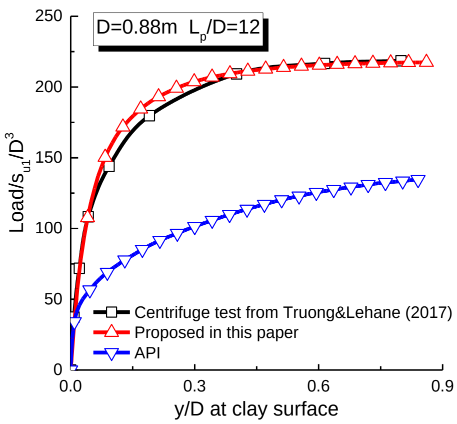

Fig. 22 Comparison between the normalized load-displacement responses

PISA field test

The performance of the new model is further evaluated based on the field test of D = 2 m pile of the PISA project which has been reported in detail in Zdravkovi et al. (2019) and Byrne et al. (2017, 2019). The clay in the test field is a glacial till at the Cowden site, its undrained triaxial compressive s_u within the depth range of 0-12 m is between 50 and 160 kPa, and behaves as a strongly nonlinear distribution with depth. The shear strength profile was detailedly reported by Zdravkovi et al. (2019a, 2019b) and Byrne et al. (2017, 2019), and it is not duplicated herein. A value of G_0/p' = 1100 (Byrne et al., 2017; Zdravkovi et al., 2019a) is assumed representative of the maximum shear modulus of soil, and the pile of 2 m in diameter is labeled as 'CL1' with a Young's modulus of 200 GPa (Zdravkovi et al., 2019a). Fig. 23 exhibits the load-displacement responses of the test pile. Similar to those mentioned above, the API's curve significantly underrates the lateral resistance of the pile, but the developed soil reaction model has a better agreement with the result of the field experiment. One point needs to note that a creep effect of the 'CL1' pile is investigated in the real field test, and the constant load plateaus can be found in the load-displacement curve of the field test. However, the results from the developed model and the one of API are from monotonic pushover analysis and are not involved with the creep effect. This is the main source of error between the field test result and the paper's result. From the Fig. 23, the reloading stiffness of test curve is closer to the one of the developed model compared to the API's prediction. If no consideration of the creep effect in real load-displacement curve, the result of the developed model is basically consistent with the field test, that is, the prediction capability of the developed soil reaction model is ensured.

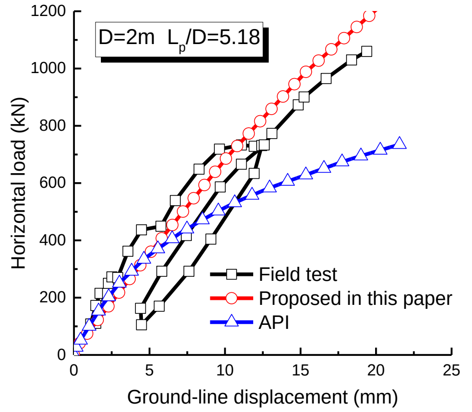

Fig. 23 Comparison between different load-displacement curves

CONCLUSIONS

Considering that the present *p*-*y* method is inappropriate to predict the lateral response of a large-diameter OWT foundation, this study discusses in detail the effects of rotational soil flow and additional resistance components on the soil-pile lateral behavior, and develops a new soil reaction model. Then, its validation is verified by centrifuge and field tests. The conclusions based on the above analyses can be drawn as follows:

1) A rotating soil flow has a significant influence on the profile of the ultimate resistance coefficient N_p. The distribution of N_p is very similar to a locus of a hyperbolic tangent function within the rotating soil flow zone, and is different from the wedge-full-flow failure. Thus, the sole consideration of wedge-full-flow failure mechanism for pile foundation design is may be inappropriate. Additionally, the value of N_p reduces with the increasing pile diameter. For instance, the maximum N_p of D = 8 m decreases nearly 15% compared to that of D = 0.91m. Furtherly, the empirical equations of N_p are proposed for taking into account these points mentioned above.

2) Based on the results from the well-calibrated FEA, it is concluded that the stiffness of the *p*-

y spring is mainly related to the L_p/D ratio rather than the pile diameter; when the L_p / D ratio is smaller (stiffer), the initial stiffness of p-y curve is larger. This implies that the p-y curves originating from the field tests of a slender pile of Matlock (1970) exist questions about the extending to a monopile design of an OWT.

3) The shear force and moment at the pile toe are significant to the lateral resistance of a large diameter pile, their total contribution is probably exceeding 20%, and leads to the findings that the use of API's (2014) p-y method obviously underestimates the lateral stiffness and the ultimate lateral resistance of large diameter monopile with relatively small slenderness ratio. Thus, these additional components of soil resistance should be considered in pile design for a more rational prediction of dynamic responses of OWT.

4) The ultimate lateral resistance of a monopile will be overestimated if a rotational flow soil mode is neglected, as a result, using a traditional p-y method based on the wedge-full-flow failure mechanism is not conservative for a design of large-diameter monopile of OWT.

5) A new soil reaction model that incorporates lateral p-y, moment (M_{base}-θ) and shear (T-u) springs is presented, and can consider the effects of three soil flow mechanisms, different pile diameters and components of base lateral resistances. Based on verification by centrifuge and field tests, this model exhibits a better predictive capability than the API's model.

ACKNOWLEDGEMENTS

This work is supported by the National Natural Science Foundation of China (Grant Nos. 51878103 and 51778092) and Innovation Group Science Fundation of the Natural Science Fundation of Chongqing, China (Grant No.cstc2020jcyj-cxttX0003).

REFERENCES

ABAQUS Inc. 2006. ABAQUS user subroutines reference manual. USA: Dassault Systerms Simulia Corp.

Achmus, M., Thieken, K., Saathoff, J. E., et al. 2019. Un- and reloading stiffness of monopile foundations in sand. Applied Ocean Research, **84**, 62–73.

American Petroleum Institute (API). 2014. Petroleum and natural gas industries-specific requirements for offshore structures. Part 4-geotechnical and foundation design considerations ISO 19901–4:2003 (Modified).

Anderson, J. B., Townsend, F. C., Grajales, B. 2003. Case history evaluation of laterally loaded piles. Journal of geotechnical and geoenvironmental engineering, **129**(3): 187-196.

Ashford, S. A., Juirnarongrit, T. 2005. Effect of Pile Diameter on the Modulus of Subgrade Reaction. Report No. SSRP-2001/22. San Diego: Department of Structural Engineering. University of California.

Byrne, B. W., McAdam, R. A., Burd H, et al. 2015. New design methods for large diameter piles under lateral loading for offshore wind applications. 3rd International Symposium on Frontiers in Offshore Geotechnics (ISFOG 2015), Oslo, Norway, June2015. p. 10-2.

Byrne, B.W., McAdam, R. A., Burd, H., et al. 2017. PISA: new design methods for offshore wind turbine monopiles. In: Proceedings of the Society for Underwater Technology Offshore Site Investigation and Geotechnics 8th International Conference, London.

Byrne, B. W., Mcadam, R. A., Burd H J, et al. 2019 Monotonic laterally loaded pile testing in a stiff glacial clay till at Cowden. Géotechnique,1-40.

Cao, G. W., Chen, Z. X., Wang, C. L., Ding, X. M. 2020. Dynamic responses of offshore wind turbine considering soil nonlinearity and wind-wave load combinations. Ocean Engineering, **217**.

Chen, Y. J., Kulhawy, F. H. 1993. Undrained strength interrelationships among CIUC, UU, and UC tests. J. Geotech. Engng, **119**, No. 11, 1732–1750.

Damgaard, M., Bayat, M., Andersen, L. V., et al. 2014. Assessment of the dynamic behaviour of saturated soil subjected to cyclic loading from offshore monopile wind turbine foundations. Computers & Geotechnics, **61**(sep.):116-126.

Doherty, P., Gavin, I. C. 2011. Laterally loaded monopole design for offshore wind farms. Proceedings of the ICE-Energy, 2011,**165**(1):7-17.

DNVGL. 2018. DNVGL-ST-0126-Support Structure for Wind Turbines. Det Norske Veritas, Oslo.

EWEA, 2016. The European offshore wind industry. Key Trends Stat 2017, **33**, 2016.

Fei K and Peng J. 2017. ABAQUS geotechnical engineering examples. The People's Posts and Telecommunications Press. (in Chinese)

Fan, C. C., and Long, J. H. 2005. Assessment of existing methods for predicting soil response of laterally loaded piles in sand. Computers and Geotechnics, **32**, pp. 274-289.

Finn, W. L., Dowling, J. 2015. Modelling effects of pile diameter. Canadian Geotechnical Journal, **53**(1): 173-178.

He, B. 2016. Lateral Behaviour of Single Pile and Composite Pile in Soft Clay. Ph.D. dissertation. Zhejiang University.

Hong, Y., He, B., Wang, L. Z., et al. 2017. Cyclic lateral response and failure mechanisms of semi-rigid pile in soft clay: centrifuge tests and numerical modelling. Canadian. Geotechnical.

Journal. **54** (6): 86–824.

Hyodo, M., Yamamoto, Y., Sugiyama, M. 1994. Undrained cyclic shear behaviour of normally consolidated clay subjected to initial static shear stress. Soils and Foundations, 1994, **34**(4):1-11

Georgiadis, M., Anagnostopoulos, C., Saflekou, S. 1992. Cyclic Lateral Loading of Piles in Soft Clay, Geotechnical Engineering, **23**.

Guo, F., Lehane, B. M., Ju, J. 2014. Experimentally derived CPT-based p-y curves for soft clay. CPT 14.

Lehane, B. M., O'loughlin, C. D., Gaudin, C, et al. 2009. Rate effects on penetrometer resistance in kaolin. Geotechnique, **59**(1): p.41-52

Liyanapathirana, D. S., Nishanthan, R. 2016. Influence of deep excavation induced ground movements on adjacent piles. Tunnelling & Underground Space Technology Incorporating Trenchless Technology Research, **52**(Feb.):168-181.

Kenneth, Gavin, Paul, Doherty. 2012. Laterally loaded monopile design for offshore wind farms. Proceedings of the Institution of Civil Engineers-Energy. **165**:7–17.

Kim, Y., and Jeong, S. 2011. Analysis of soil Resistance on laterally loaded piles based on 3D soil-pile interaction. Computers and geotechnics, **38**(2): 248-257.

Lau, B.H. 2015. Cyclic behavior of monopole foundations for offshore wind turbines in clay. Doctoral dissertation. University of Cambridge.

Luan, L. B., Zheng, C. J., Kouretzis, G., et al. 2020a. Dynamic analysis of pile groups subjected to horizontal loads considering coupled pile-to-pile interaction. Computers and Geotechnics, **117**: 103276.

Luan, L. B., Ding, X. M., Zheng, C. J., et al. 2020b. Dynamic response of pile groups subjected to horizontal loads. Canadian Geotechnical Journal, **57**(4): 469-481.

Jeanjean, P. 2009. Re-assessment of P-Y curves for soft clays from centrifuge testing and finite element modeling. In Offshore Technology Conference, Offshore Technology Conference.

Jung, S., Kim, S. R., Patil, A., et al. 2015. Effect of monopile foundation modeling on the structural response of a 5-MW offshore wind turbine tower. Ocean Engineering, **109**(NOV.15):479-488.

Martin, C.M., and Randolph M.F. 2006. Upper-bound analysis of lateral pile capacity in cohesive soil. Geotechnique, **56**(2):141-145.

Matlock. 1970. Correlations for design of laterally loaded pile in clay. Proceedings of the Offshore Technology Conference, Houston, Paper OTC1204, pp.577-588.

Murff, J. D., Hamilton, J. M. 1993. P- Ultimate for Undrained Analysis of Laterally Loaded Piles. Journal of Geotechnical Engineering, 1993, **119**(1):91-107.

Murphy, G., Igoe. D., Doherty. P., et al. 2018. 3D FEM approach for laterally loaded monopile design. Computers and Geotechnical. **100**, 76–83.

Peng Y, Liu H L, Li C, et al. 2020. The detailed particle breakage around the pile in coral sand. Acta Geotechnica: 26–35. Accepted.

Poulos, H. G., Hull, T. S. 1989. The role of analytical geomechanics in foundation engineering, Foundation Engineering @Current Principles and Practices. ASCE: 1578-1606.

Randolph, M. F. 1981. The response of flexible piles to lateral loading. Geotechnique, **31**(2): 247-259.

Reese, L. C. and R. C. Welch. 1975. Lateral loading of deep foundations in stiff clay. Journal of Geotechnical & Geoenvironmental Engineering, **101**(7): 633–649.

Sloan, S. W. 1987. Substepping schemes for the numerical integration of elastoplastic stress-strain relations. International Journal for Numerical Methods in Engineering, **24**(5): 893-911

The, C. I., Houlsby, G. T. 1991. An analytical study of the cone penetration test in clay. Geotechnique, **41**(1): 17-34

Templeton, J. 2009. Finite element analysis of conductor/seafloor interaction. Proceedings of the offshore technology conference, Houston, TX, USA, paper OTC-20197.

Truong, P., Lehane, B. M., 2017. Effects of pile shape and pile end condition on the lateral response of displacement piles in soft clay. Geotechnique, **68**(9):794-804.

Tzivakos, K. P., Kavvadas, M. J., 2014. Numerical investigation of the ultimate lateral resistance of piles in soft clay. Frontiers of Structural and Civil Engineering, **8**(2):194-200.

Wang, L., Lai, Y., Hong, Y., et al, 2020. A unified lateral soil reaction model for monopiles in soft clay considering various length-to-diameter (L/D) ratios. Ocean Engineering, **212**:107492.

Wroth, C. P. 1985. Soil mechanics - Property characterization and analysis procedure. Proc. int. conf. smfe, 1.

Yu, H. S., Houlsby, G. T., 1990. Cavity expansion theory and its application to the analysis of pressuremeters. University of Oxford.

Yu, J., Huang, M., Leung, C. F., et al. 2017. Upper bound solution of a laterally loaded rigid monopile in normally consolidated clay. Computers & Geotechnics, **91**(nov.):131-145.

Yu, J., Huang, M. S., Zhang, C. 2015. Three-dimensional upper-bound analysis for ultimate bearing capacity of laterally loaded rigid pile in undrained clay. Canadian Geotechnical Journal, **52**(11):150417143448009.

Zdravkovi, L., Taborda, D. M. G., Potts D M, et al. 2019a. Finite element modelling of laterally loaded piles in a stiff glacial clay till at Cowden. Géotechnique,1-40.

Zdravkovi L, Jardine R J, Taborda D M G, et al. 2019b. Ground characterisation for PISA pile testing and analysis. Géotechnique, 1-50.

Zhang, Y. H., Andersen, K. H. 2019. Soil reaction curves for monopiles in clay. Marine Structures. **65**, 94–113.

Zhou, C., Ng, C. W, W. 2015. A thermomechanical model for saturated soil at small and large strains. Canadian Geotechnical Journal, **52**(8), 150107143558000.

Zhou, P., Zhou, H., Liu, H. L., et al. 2020. Analysis of lateral response of existing single pile caused by penetration of adjacent pile in undrained clay. Computers and Geotechnics, **126**:103736.

Zhu, B., Zhu, Z. J., Li, T., et al. 2017. Field tests of offshore driven piles subjected to lateral monotonic and cyclic loads in soft clay. Journal of Waterway Port Coastal & Ocean Engineering, **143**(5), 05017003.